Permeability simulation for filled paper based on three-dimensional structural model developed by X-ray computed tomography scanning

JIAXIAN CHEN, YI WANG, YIN LIU, LI CHEN, WENHAO SHEN, JAAN-WILLEM SIMON, AND YAN HUANG

ABSTRACT: In this study, an in-depth exploration of filled paper was conducted to understand its structural and permeability characteristics. Cotton linter pulp and precipitated calcium carbonate (PCC) filler were utilized to prepare pure fiber paper, and PCC1 and PCC2 filled papers with different filler particle sizes. Then, the pore structure parameters of paper samples were characterized by mercury intrusion porosimetry, and the X-ray computed tomography (X-CT) scanning was carried out. Subsequently, the 3D microstructures were established based on the X-CT slice images, and the filler characteristic parameters and filler 3D distribution were quantitatively analyzed. Finally, permeation simulations in the thickness and horizontal directions were performed.

The findings indicate that filling changes the paper porosity, and the pore tortuosity varies with direction. The estimated pore–throat radius distribution shows specific patterns for different papers. The fillers have different distribution characteristics in the paper samples. Moreover, the paper permeability differs with direction, with small-sized filler having a significant impact on fluid penetration in the thickness direction. Overall, this study provides an effective method for investigating internal paper filler and its distribution, which contributes to the understanding of paper structure–performance relationships.

Application: This research offers an effective exploratory approach for investigating paper fillers from the perspective of computer simulation, facilitating the structural design and performance optimization of paper-based functional materials.

As a porous material, paper primarily utilizes plant fibers as raw constituents [1]. The processing techniques for paper have been in a continuous state of evolution, concomitant with modifications in its structural and performance attributes. As a customary processing approach, filling use has been widely applied, incorporating fillers into many paper grades. Their usage quantity secures them the second position among papermaking raw materials, trailing only behind papermaking fibers [2]. During the formation process of wet paper, fibers and fillers are jointly retained on the web, thereby inducing alterations in the three-dimensional (3D) network architecture and diverse physical properties of paper.

Filling entails the introduction of a specific proportion of inorganic or organic fillers into the pulp. Generally, this practice confers several benefits: (1) lower cost of papermaking fillers compared to that of paper fibers, facilitating a reduction in production costs; (2) enhancement of the optical properties of paper, such as augmenting whiteness and opacity; and (3) occupation of the interstitial spaces between fibers within the paper web, improving dewatering efficiency, optimizing paper formation, and promoting uniformity [3]. The filler characteristics that influence the performance of filled paper include: particle size and its distribution profile, specific surface area, particle morphology, and spatial distribution of particles in the paper web. Notably, filler distribution significantly impacts paper permeability [4], and different paper types have distinct distributions in the thickness direction, which refers to the *z*-direction. To elucidate the disparities in paper performance associated with different filler *z*-distributions [5], it is imperative to comprehensively understand the filler distribution along the *z*-direction of the paper.

The elements of particle size, size distribution, and other attributes of fillers play an important role in shaping the 3D structure and ultimate performance of the paper. Hence, investigating the 3D structure of filled paper lays a solid foundation for probing the intricate relationship between its structure and performance. With the technology development, several 3D characterization techniques have been enlisted for the structural elucidation of paper fiber networks. Presently, technologies such as confocal laser scanning microscope (CLSM), focused ion beam-scanning electron microscope (FIB-SEM), and X-ray computed tomography (X-CT) have garnered significant attention [6], providing essential knowledge for understanding the prop-

erties of paper. In comparison to CLSM and FIB-SEM, X-CT offers the unique advantage of high-precision 3D non-destructive imaging, thereby driving significant progress in simulation research on the structures and properties of fiber-based porous media. By contrast, since the operation of CLSM depends on sample transparency, which is heavily influenced by the scattering coefficient of fillers, it is ineffective for the purposes of this study.

A non-destructive 3D imaging technique, X-CT has its origins in medical and biological fields [7]. Operating on the principle of X-ray interaction with matter, it retrieves internal compositional and structural information of the inspected object through projection reconstruction. Its efficacy in revealing the 3D structure of paper fiber networks has been well-established [8]. FIB-SEM is suitable for generating coating sections, but it is not ideal for visualizing a detailed 3D pore structure [9]. Samuelsen was the first to obtain non-destructive cross-sectional images of paper interiors using X-CT [10]. Ahmad et al. utilized X-CT scanning imaging technology to contrast the pore structures of foam-formed fiber paper and traditional handcrafted paper [11]. Notably, Ramaswamy et al. further employed X-ray microtomography to reconstruct the 3D pore-fiber structure of paper, analyzing its relationship with moisture transport and highlighting the anisotropic pore characteristics in different directions [12]. Thus, the aforementioned studies demonstrate that X-CT has been an effective technique for analyzing the internal structure of paper, particularly for revealing the 3D architecture of fiber networks and pore structures.

The advances in microscopic imaging, image processing, computer simulation, and computational capabilities have spurred the development of computer simulation methodologies for investigating internal fluid permeation behavior in materials preparation, reinforcement, and structural design. In recent years, some scholars have initiated the research on permeability of fillers and pulp fiber mats. Lavrykov discovered that filler addition influenced the filtration time of pulp fiber mats [13], and Singh pioneered the exploration of the permeability of pulp fiber networks [14]. Also, Pan developed a 3D structural model of paper-based filter materials by combining X-CT and FIB-SEM technologies and predicted the filtration performance [15]. Given that the fiber structure and physical properties of wet paper undergo significant changes during the subsequent formation process, it is essential to study the permeability of the formed paper web.

In the study, the evolution of filler characteristics after filler application in the paper web and its impact on the permeation behavior of filled paper are investigated. Targeting the nontransparent filled paper and the nondestructive characterization, the X-CT scanning technology was employed to establish the 3D structural models. Three samples were considered in the study, unfilled paper and two filled papers with different filler particle sizes, and the permeation simulations were conducted accordingly. With the developed 3D structural models, the study results reveal two points: (1) the characteristics and spatial distributions of pore, fiber, and filler in the interior of paper web can be obtained based on the three extracted components; and (2) the relationship between the structure and permeation performance can be further established, offering a valuable insight for the structure-performance study of the paper web.

Average Length, mm	Weight-Average Length, mm	Width, μm	Coarseness, mg/m
0.549	0.818	32.3	0.1396

I. Main properties of the cotton pulp.

EXPERIMENTAL

In this study, cotton linter pulp and precipitated calcium carbonate (PCC) filler were used as raw materials, and cationic polyacrylamide (CPAM) served as a pre-flocculation modifier. The characteristics of the cotton linter pulp are shown in **Table I**.

Preparation and characterization of filled paper

The PCC filler was prepared as a 1% mass fraction of filler suspension, designated as PCC1. The suspension was subjected to magnetic stirring at a rate of 300 rpm for 5 min. Subsequently, a CPAM solution with a concentration of 0.02% (based on the mass of PCC) was added to the PCC1 suspension, and the mixture was stirred for an additional 5 min to produce the pre-flocculated filler suspension, designated as PCC2. The particle sizes of the fillers in PCC1 and PCC2 suspensions were measured using a laser particle size meter (LA-960S, HORIBA; Kyoto). It should be mentioned that the employed pre-flocculation process in the study was used to increase the apparent particle size of the fillers rather than to modify the filler, therefore studying the effects of different filler particle sizes on the 3D network structure of the paper.

The cotton linter pulp was disintegrated and subsequently beaten to a beating degree of 30 ± 2 °SR using a beater (Valley, IMT Instruments; Dongguan City, China). One 3.30-g portion of the pulp was disintegrated, formed into paper, and dried (RK3AKWT, Frank-PTI; Birkenau, Germany) to produce a pure fiber paper (with a basis weight of 105 ± 1 g/m²), serving as a blank reference. For the filled paper samples, 2.80 g of the pulp was combined with either filler PCC1 or PCC2 (at an addition rate of 15%), disintegrated, formed into paper, and dried to achieve two types of filled paper with the basis weight of 105 ± 1 g/m². The dried papers were stored in a constant temperature and humidity chamber maintained at 25°C and 50% relative humidity for subsequent use.

The pore structure of the prepared paper samples was

characterized using a Micromeritics (Norcross, GA, USA) AutoPore IV 9500 automated mercury intrusion porosimeter (MIP), enabling the determination of parameters such as porosity, pore fractal dimension, pore tortuosity, and permeability.

X-ray CT scanning

The prepared samples of pure fiber paper, filled paper PCC1, and filled paper PCC2 were cut into 1 mm × 1 mm dimensions and affixed to the sample stage of an X-CT scanner (SkyScan 2211, Bruker; Billerica, MA, USA) for scanning. The scanning mode was set to the nano-resolution mode with a source voltage of 50 kV, rotation range of 0.25° to 0.30° with the rotation step of 0.3°, an exposure time of 800–950 ms, and a pixel size of 400 nm.

The X-CT scanning acts on the basis of detecting the energy attenuation of X-rays within the sample. Different elements have different absorption coefficients for X-rays. Notably, the elements with high atomic numbers tend to have high absorption rates of X-rays, which consequently leads to relatively high grayscale values in the resultant images due to their low transmission of radiation.

THREE-DIMENSIONAL MODELING AND NUMERICAL SIMULATION METHODS

This section undertakes the preprocessing of X-ray CT scan 2D images obtained in the Experimental section under "Construction of 3D structural models of paper." Subsequently, the pore structure parameters (porosity, pore tortuosity, and pore fractal dimension) and the filler characteristic parameters (filler particle size, specific surface area, and spatial distribution) are estimated, and the corresponding conditions are established for conducting permeation simulation in thickness and horizontal directions. The roadmap is illustrated in **Fig. 1**.

Construction of 3D structural model of paper

The original 2D X-ray CT slice images were acquired in the X-Z plane by X-CT scanning. To improve the image quality (contrast and substantial noise), image processing was implemented prior to the 3D digital model construction. The non-local means (NL-means) filter was employed for noise reduction, leveraging patch-based similarity to suppress noise while preserving texture details. Specifically, for each pixel, the algorithm computed a weighted average of similar patches within a search window, where weights were determined by patch similarity using a Gaussian kernel. The parameters used for the NL-means filter were as follows: the search window radius was set to 4.5 (resulting in a search window size of 9); the similarity window radius was set to 1 (resulting in a similarity window size of 3); and the filter strength parameter was set to control the balance between noise reduction and detail preservation. Subsequently, the Otsu dual-threshold segmentation algorithm was used to divide the images into the phases of pore, fiber, and filler based on the gray variance among different components of the paper. The Otsu algorithm automatically determines the two optimal thresholds by maximizing between-class variance. The segmentation was performed using the software of MATLAB R2021a (MathWorks; Natick, MA, USA).

The processed 2D slice images were imported into Avizo software (Thermo Fisher Scientific; Waltham, MA, USA) for 3D structure modeling. Due to the limitations of both radiographic imaging and computing power, the concept of the representative volume element (RVE) is introduced for the subsequent analysis and permeation simulation, which represents the smallest unit cell that yields representative results in a statistical sense [16]. Specifically, the RVE size was determined by balancing geometric statistical deviation (e.g., 5% standard deviation for porosity and specific surface

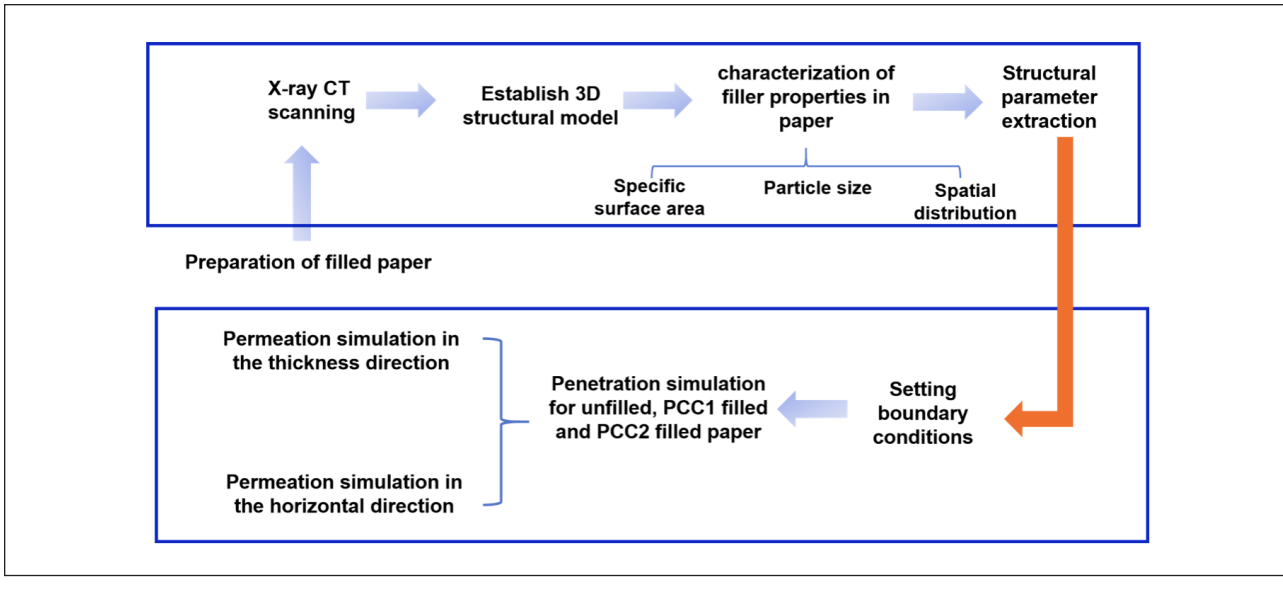

1. Technical roadmap of the study (CT: computed tomography; 3D: 3 dimensional; PCC: precipitated calcium carbonate).

area) and the Brinkman screening length criterion, ensuring consistency between microstructural representativeness and macroscopic transport property simulation.

The RVE size is determined by the estimated parameters such as porosity, pore tortuosity, and pore fractal dimension, in which the porosity and pore fractal dimension are calculated by the volume fraction and fractal dimension modules in Avizo software, respectively, and the pore tortuosity in the z-direction is obtained through the generated pore network model function [17]. These parameters are defined as follows:

1. Porosity quantifies the relationship between the pore and solid phases in the paper sample, which is closely associated with the mechanical strength and fluid transport property of poral material.
2. Pore tortuosity, a crucial characteristic parameter of pore structure, describes the path traversed by liquids or gases during transport, having significant influence on the transport performance of material.
3. Pore fractal dimension characterizes the geometric complexity of pore structure and impacts the mechanical strength and fluid transport behavior of porous material. This approach aligns with the method where correlations between pore structure parameters and REV size are established to determine the unified REV size [18].

Extraction of filler parameters from 3D structural model

Based on the determined RVE, through digital image processing techniques, the parameters of applied filler in paper were estimated and quantitatively analyzed. A workflow for extracting the characteristics (filler particle size distribution, specific surface area, and spatial distribution) from the X-CT images of filled paper was established, whose specific steps are as follows:

1. The X-CT images of filled paper segmented by the Otsu dual-threshold method were imported into Avizo software, and the interactive thresholding module was used to extract the filler particles based on its gray value of 255.
2. The label analysis module was utilized to sample and analyze the estimated filler particles, extracting the parameters of particle size, area, volume, and the 3D position of filler, in which the specific surface area was calculated by defining it as the ratio of area to volume.
3. The volume rendering command was applied to perform 3D volume rendering on the estimated filler particles so that the distribution of the filler particles in the internal 3D space of paper can be observed visually.

Permeation simulation for filled paper

To make the simulation be consistent with the experimental method, i.e., mercury intrusion porosimetry, the fluid of liquid mercury is used for the simulation, which is assumed to be incompressible, stable, and viscous. The simulation principle and boundary setting conditions are discussed here.

The governing equation employed in the permeation simulation is the recognized Navier-Stokes equation [19], including mass conservation equation (Eq. 1) [20] and momentum conservation equation (Eq. 2) [21]:

$$\rho(\vec{v}\cdot\nabla\vec{v}) = -\nabla p + \mu\Delta\vec{v} + \vec{f} \quad (1)$$

$$\nabla\vec{v} = 0 \quad (2)$$

where ρ is fluid density, $\vec{v}$ is flow velocity, p is pressure, μ is fluid viscosity, and $\vec{f}$ is the external force of zero under gravity action.

In addition, prior to the permeability simulation for filled paper, boundary conditions (physical conditions on the boundary) require definition. In this study, three types of boundary conditions are considered in the permeability simulation: pressure boundary condition, solid wall boundary condition, and symmetric boundary condition. In general, the inlet/outlet pressure boundary condition is used for fluids with unknown inlet flow velocity [22]; the solid wall boundary condition is applied to distinguish the boundary between the fluid domain and the solid domain; and the symmetric boundary condition is employed to reduce the size of the computational domain, improve efficiency, and ensure accuracy.

Based on the determined RVE, permeation simulations of paper were conducted in the thickness direction and the horizontal direction, respectively. The inlet pressure P_{in} was set to 300 Pa, and the outlet pressure P_{out} was zero, which opened to air. The boundary conditions for the external surfaces of RVE are set as symmetric boundaries, and the interfaces between the fibers and pores are set as solid wall boundary conditions. The detailed settings of boundary conditions are shown in **Table II** and **Fig. 2**.

Condition	Description	Inlet/Outlet	Symmetric Boundaries	No-Slip Solid Wall Boundaries
Case 1	Single outlet in the thickness direction	A/B	C, D, E, F	Internal fiber-pore intersection
Case 2	Single outlet in the horizontal direction	C/D	E, F	A, B, internal fiber-pore intersection

II. Defined boundary conditions for the permeation simulations of filled paper.

RESULTS AND DISCUSSION

Development of 3D structural model for filled paper

Processing of 2D X-CT scanning image

As shown in **Fig. 3**, after the X-CT scanning of unfilled paper (resolution of 3000 × 700 pixels), PCC1 filled paper (resolution of 3000 × 600 pixels), and PCC2 filled paper (resolution of 3000 × 600 pixels), tomographic slice images (2102-pixel sequences of 8-bit 2D grayscale) along the *x*–*z* direction were obtained for each paper sample.

Prior to the 3D digital model construction, to improve the contrast and decrease the substantial noise of the obtained 2D images, the image processing was conducted by the methods described in the Experimental section under

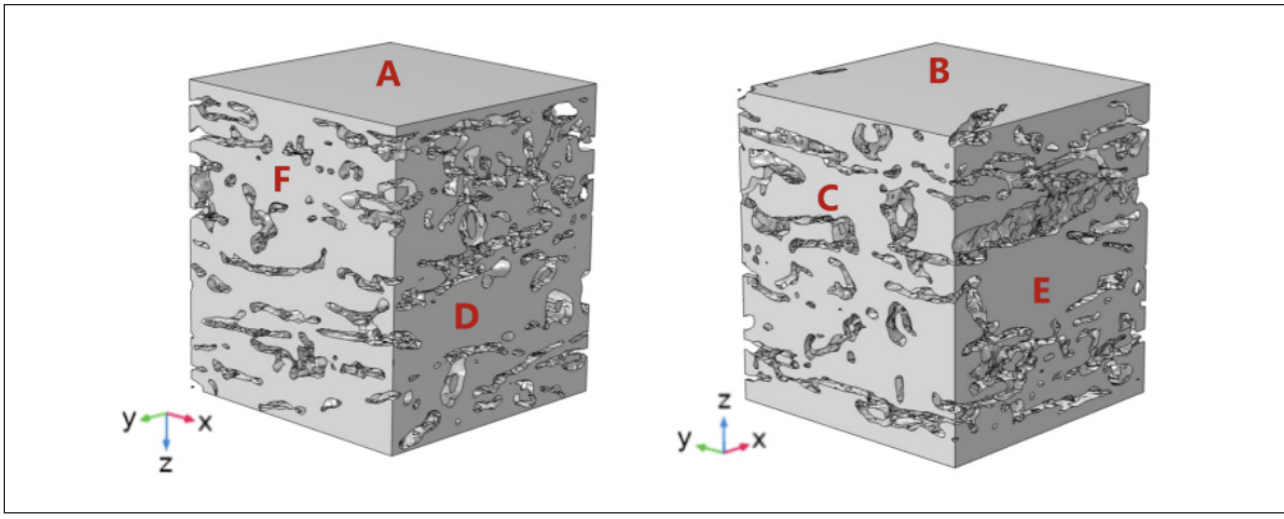

2. Schematic of the boundary labeling of representative volume element (RVE) for the permeation simulation.

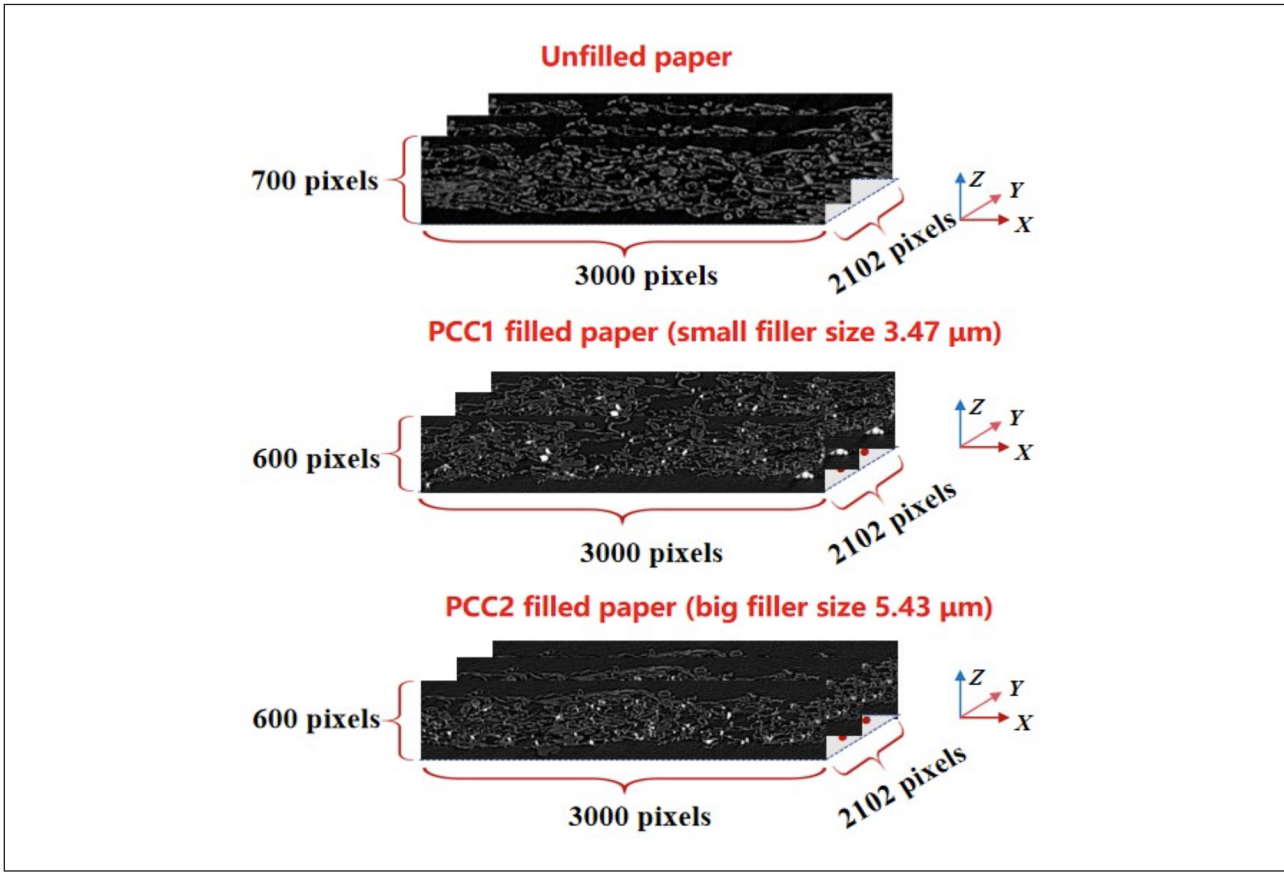

3. Tomographic slice image sequences of unfilled paper, PCC1 filled paper, and PCC2 filled paper obtained by X-ray computed tomography (X-CT) scanning.

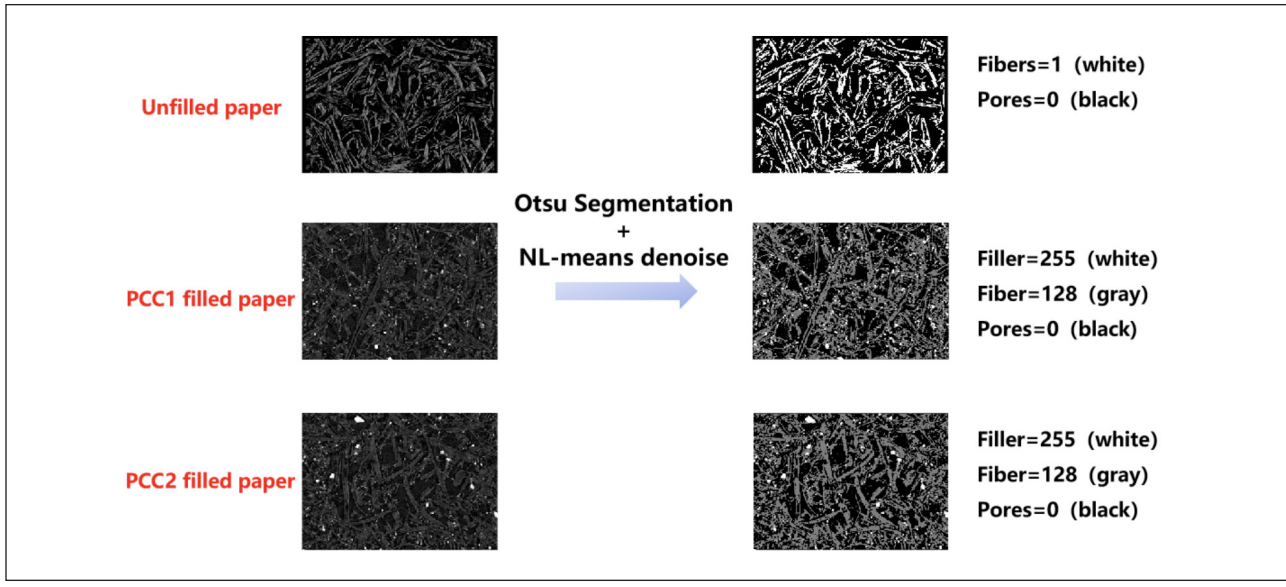

4. Processing of two-dimensional (2D) X-CT scanning images of unfilled paper and PCC1 and PCC2 filled papers.

"Construction of 3D structural model of paper." As displayed in **Fig. 4**, the processed results indicate that, with the strategies of Otsu segmentation and NL-means denoise, the filler, fiber, and pore are effectively separated. After separation, the grayscale values of the components of filler, fiber, and pore in Fig. 4 are 255, 128, and 0, respectively.

Establishment of 3D structural models

After image processing, the 2D X-CT scanning slice images in the *x*–*y* direction are imported into Avizo software for the development of the 3D structural model. Along the *z*-direction of paper web, the volume rendering module of Avizo software was applied to reconstruct the isosurface and was followed by performing 3D volume rendering to construct the 3D structural models of paper web.

The constructed 3D structural models for unfilled paper, PCC1 filled paper, and PCC2 filled paper are shown in **Fig. 5**. It can be observed from Fig. 5 that, under the same grammage, the application of filler results in the reduced thickness for both PCC1 and PCC2 filled papers,

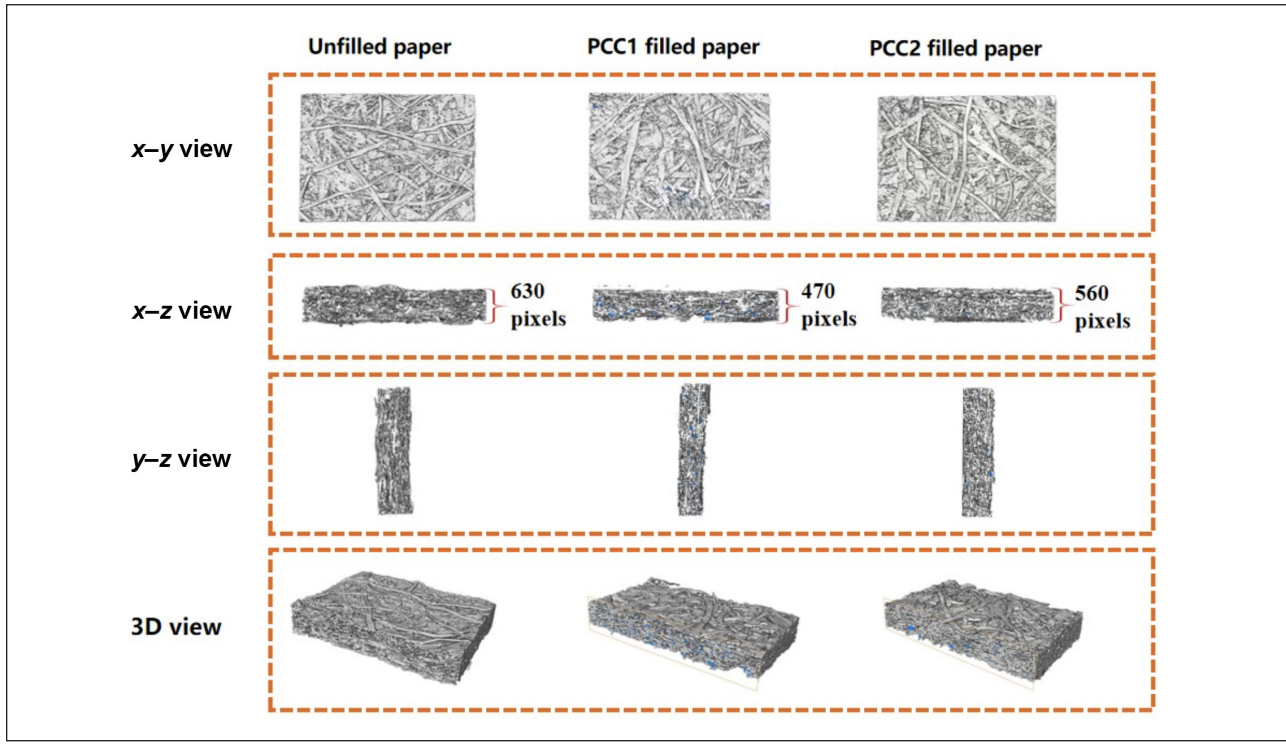

5. Three-dimensional (3D) structural models of unfilled paper and PCC1 and PCC2 filled papers.

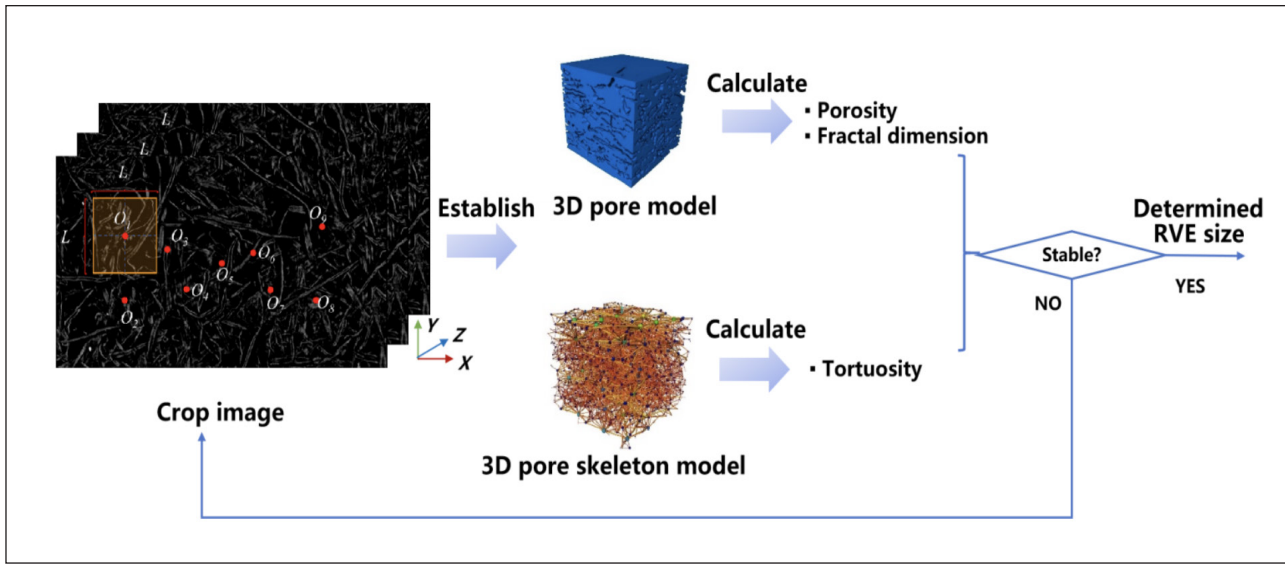

6. Schematic diagram of the method for determining RVE size.

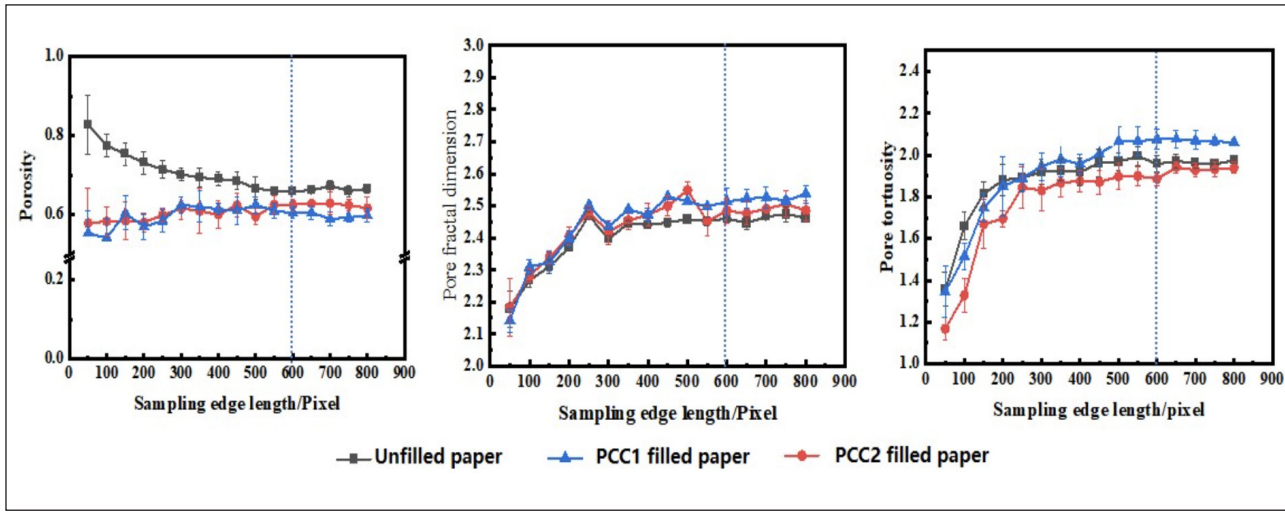

7. Relationship between the side length of RVE for three kinds of paper and porosity, pore fractal dimension, and pore tortuosity.

decreasing from 630 pixels for unfilled paper to 470 pixels for PCC1 and 560 pixels for PCC2. The bulk of the two filled papers also showed a decline. This can be explained by the fact that, with a constant grammage (105 ± 1 g/m²), the addition of fillers leads to a reduction in the number of fibers in the matrix, and therefore, the decreased thickness of the filled papers. Moreover, applying the same filler addition of 15%, compared to PCC2 with larger particle sizes, the small filler particles of PCC1 tend to fill the interstitial spaces between fibers more effectively, while the large filler particles of PCC2 can expand the fiber interstices. Consequently, the paper web with larger filler particles (PCC2) demonstrates a greater thickness than that of PCC1.

As described in the Experimental section under "Construction of 3D structural models," the RVEs require determination to save computing power for the subsequent permeation simulation. The method for determining RVE is illustrated in **Fig. 6**, in which the side length of RVE was set to range from 50 pixels to 800 pixels, retaining their thickness, and the estimated parameters (porosity, pore tortuosity, and pore fractal dimension) were used to determine the RVE size. When enlarging the side length in the plane of RVE with an increment of 50 pixels (Fig. 6), the evolutions of the estimated porosity, pore tortuosity, and pore fractal dimension of RVE are given in **Fig. 7**. It can be observed that, with the increased side length, all three parameters of the unfilled paper and PCC1 and PCC2 filled papers tend to be stable when their side lengths reach 600 pixels. Therefore, the determined RVE dimensions are as follows: 600 × 600 × 630 pixels for the unfilled paper, 600 × 600 × 470 pixels for the PCC1 filled paper, and 600 × 600 × 560 pixels for the PCC2 filled paper.

Characterization of filled paper with established 3D structural model

Pore structure characterization of filled paper

Based on the determined RVE dimensions, using the method described in the Experimental section regarding "Construction of 3D structural models of paper," the pore structures of the unfilled paper and the PCC1 and PCC2 filled papers were characterized with the estimated parameters of porosity, pore tortuosity, and fractal dimension. In addition, these estimated values were compared with the experimental results (porosity, pore tortuosity in *z*-direction, and fractal dimension) by the AutoPore IV 9500 automated MIP.

Before the parameter extraction of pore structure, the pore skeleton networks of paper samples were isolated from the determined RVE using the maximum sphere algorithm [23]. As shown in **Fig. 8**, the pore structures in RVE are expressed by the network of balls and rods, where the balls represent pores and the rods represent pore throats. The colors correspond to their equivalent spherical radii. The obtained pore network skeleton models characterize the pore distribution and their connections in the paper structure virtually. The specific steps for extracting pore structure parameters (pore equivalent radius distribution, pore throat equivalent radius distribution, and pore throat coordination number) are as follows:

1. Based on the determined RVE size, the binary *x*–*y* slice images were cropped. The cropped data were imported into Avizo software.
2. The Volume Fraction and Fractal Dimension modules of Avizo software were used to calculate porosity and fractal dimension, respectively.
3. The Separate Object Module was used in the Skeleton-Aggressive mode of Avizo software to separate the pore space into pores and pore throats (pore throats are the narrow channels connecting pores in Fig. 8).
4. The Generate Pore Network Model function of Avizo software was used to create the pore skeleton network model in the *z*-direction, and the parameter of pore tortuosity in the *z*-direction was obtained from the model properties.
5. The generated pore skeleton network models were visualized by the Volume Rendering module of Avizo software, and the model properties could be obtained, including the equivalent spherical radii of individual pores and pore throats, as well as the coordination number.
6. The obtained data were exported to OriginLab software (OriginLab; Northampton, MA, USA) to plot the histograms of pore equivalent radius distribution and pore throat equivalent radius distribution.

The experimental and estimated results are compared in **Table III**. It can be observed that the experimental results of three paper samples before and after filling operation align with the estimated pore parameters from RVE, which are the porosity (unfilled 0.65/0.67; PCC1 filled 0.60/0.58; and PCC2 filled 0.61/0.60), pore tortuosity in *z*-direction (unfilled 1.77/1.98; PCC1 filled 1.89/2.05: and PCC2 filled 1.71/1.94), and fractal dimension (unfilled 2.57/2.42; PCC1 filled 2.98/2.51; and PCC2 filled 2.58/2.44). Furthermore, the estimated pore tortuosity in the horizontal directions (*x* and *y*) of the paper samples are lower than those in the *z*-direction (unfilled 1.51/1.50/1.98; PCC1 filled 1.52/1.54/2.05; and PCC2 filled 1.56/1.46/1.94), indicating that the fluid traverses a shorter path along the horizontal plane, facilitating permeation. The tortuosity in the *x* and *y* directions of the three papers are comparable (unfilled 1.51/1.50; PCC1 filled 1.52/1.54; and PCC2 filled 1.56/1.46), and no significant differences are observed in the horizontal pore tortuosity between the filled papers and the unfilled paper.

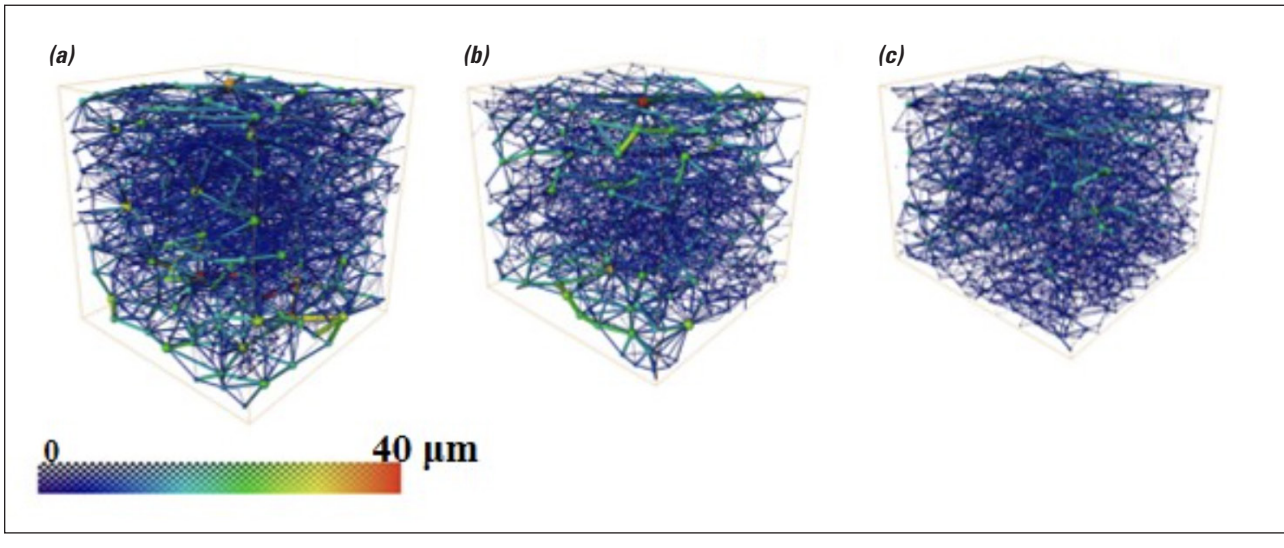

8. Pore skeleton network models of (a) unfilled paper, (b) PCC1 filled paper, and (c) PCC2 filled paper.

Parameter	Experimental Value			Estimated Value		
	Unfilled	PCC1 Filled	PCC2 Filled	Unfilled	PCC1 Filled	PCC2 Filled
Porosity	0.65	0.60	0.61	0.67	0.58	0.60
Tortuosity (*z*)	1.77	1.89	1.71	1.98	2.05	1.94
Tortuosity (*x*)	-	-	-	1.51	1.52	1.56
Tortuosity (*y*)	-	-	-	1.50	1.54	1.46
Fractal dimension	2.57	2.98	2.58	2.42	2.51	2.44

III. Comparison of pore parameters estimated from representative volume element (RVE) and experimental characterization (PCC: precipitated calcium carbonate).

Overall, in Table III, the pore parameters estimated from RVE are close to the experimental ones by MIP, demonstrating the feasibility of the X-CT scanning technique combined with digital image processing method adopted in the present study. Additionally, it is noted that the pore tortuosity in *z*-direction estimated from RVE is relatively higher than the experimental ones (unfilled 1.98/1.77; PCC1 filled 2.05/1.89; and PCC2 filled 1.94/1.71). It can be explained that, based on the measuring principle of the MIP, some tortuous sections of the pore structure cannot be completely penetrated by mercury; only those accessible pores can be detected, leading to an underestimation of the experimental pore tortuosity.

Based on the obtained pore skeleton networks of the three paper samples in **Fig. 9**, the equivalent sphere radii of pores and pore throats within the RVE were quantitatively estimated. It can be observed that the experimentally measured pore radius distribution (Fig. 9a) is similar to the distribution of the equivalent spherical radius of pores estimated by RVE (Fig. 9b). The radius of most pores lies in the range of 1–5 µm, and less distribution for the large pores can be observed. Also, all of the estimated equivalent spherical radii of pore throats (Fig. 9c) of the three paper samples are in the range of 3–5 µm. In particular, as revealed in Fig. 9b and Fig. 9c, the PCC1 filled paper with small filler particle size exhibits abundant distributions of pore and pore throat radii in the range of 1–5 µm. These phenomena are attributed to the fact that during the forming process of paper, the applied filler particles move into the area between fibers, partitioning large pores into small ones and promoting uniform pore distribution. The small filler particles are conducive to form a tightly bound paper structure with small pores interconnected by small pore throats.

Filler characterization of filled paper

Utilizing the method detailed in the Experimental section on "Extraction of filler parameters from 3D structural model," the filler characteristics in PCC1 and PCC2 filled paper were quantitatively estimated by X-CT scanning images. Employing Avizo software, 18646 (PCC1) and 7733 (PCC2) filler particles were extracted from RVEs, respec-

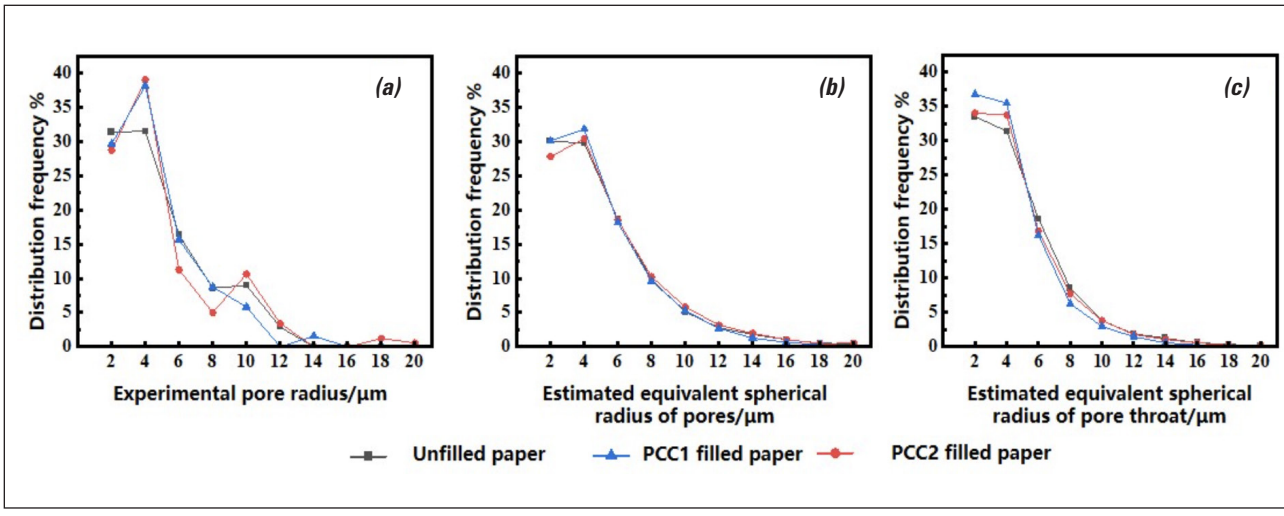

9. Distributions of pore radius and pore throat radius in the (a) unfilled paper, (b) PCC1 filled paper, and (c) PCC2 filled paper.

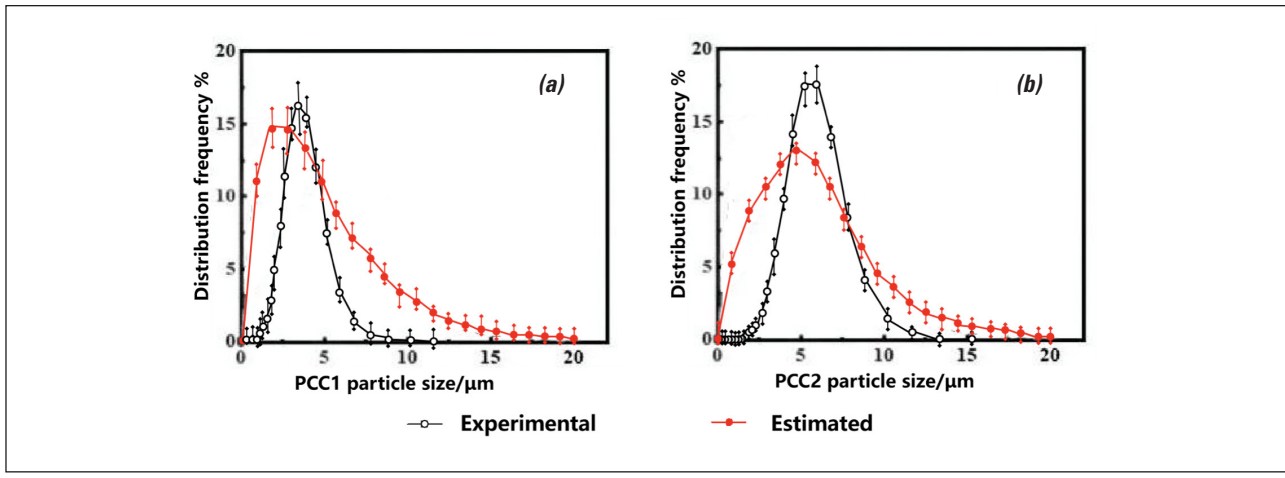

10. Experimental and estimated particle size distributions of fillers for PCC1 and PCC2.

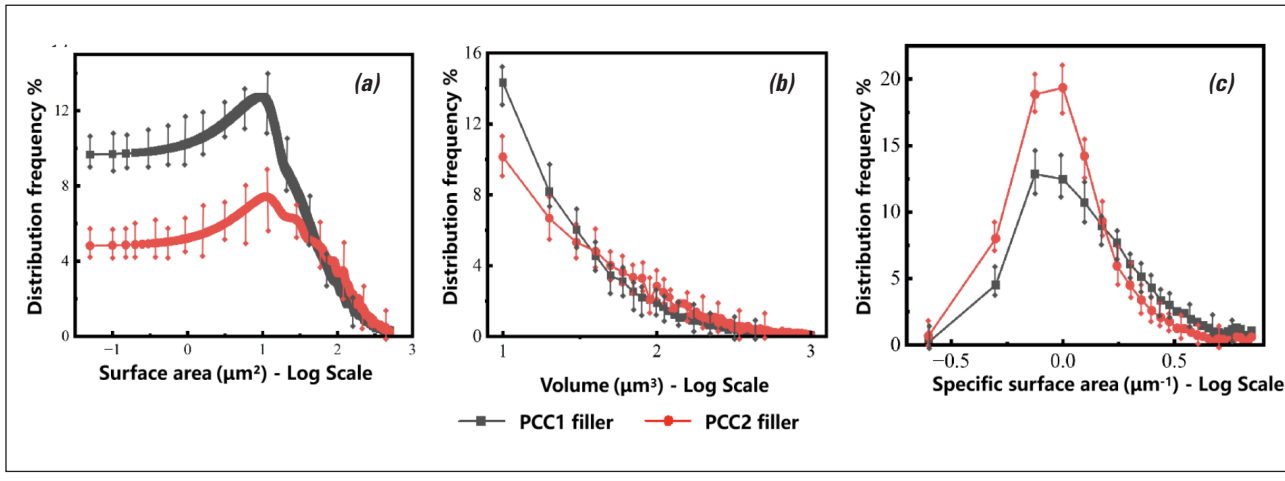

11. Estimated distribution of filler (a) surface area, (b) volume, and (c) specific surface area by X-CT analysis.

tively. The reduction of PCC2 filler particle number demonstrates the significant pre-flocculation effect of filler.

Figure 10 plots the particle size distributions of the fillers estimated from X-CT and measured by the laser particle size analyzer. The experimental particle size distribution reflects the filler particle size prior to its incorporation into paper, whereas the estimated distribution reveals the filler particle size and their distributions in the formed paper. As depicted in Fig. 10, both before and after their additions to the paper, the particle size of PCC2 filler is consistently larger than that of PCC1 filler, and PCC2 appears to exhibits a more pronounced distribution in the region above 5 μm compared to PCC1, suggesting that the pre-flocculation treatment induces the filler particle flocculation and increase of particle size. Both results with laser particle size analyzer and X-CT scanning indicate the increased particle sizes of PCC1 (3.47–4.15 μm) and PCC2 (5.43–5.45 μm) after their additions, which may have arisen from the forming process. Since the experimental and estimated data represent the filler particle size before and after the filling process, these data reveal the evolution of filler particle size, which may have arisen from the forming process. Notably, the PCC2 filler with greater particle size remains relatively stable after paper incorporation (from 5.43 to 5.45 μm); however, the low particle size of the PCC1 filler increases by 20% upon its direct addition to pulp (from 3.47 to 4.15 μm), suggesting that the filler with small particle size is more likely to undergo flocculation and subsequent size augmentation in the subsequent forming process.

In addition to the particle size distribution of fillers in paper samples, the surface area, volume, and specific surface area distributions of fillers were also estimated by X-CT scanning. The Label Analysis module in Avizo software was used to sample and analyze the filler particles within the 3D models, extracting parameters such as area, volume, and the 3D centroid positions. The specific surface area was calculated as the ratio of surface area to volume. As shown in **Fig. 11** (with data presented on a logarithmic scale), the surface area (Fig. 11a) and volume (Fig. 11b) of the PCC2 filler increase following the pre-flocculation treatment, and the specific surface area distribution (Fig. 11c) peaks of both PCC1 and PCC2 fillers are approximately 1 μm^{-1}. The

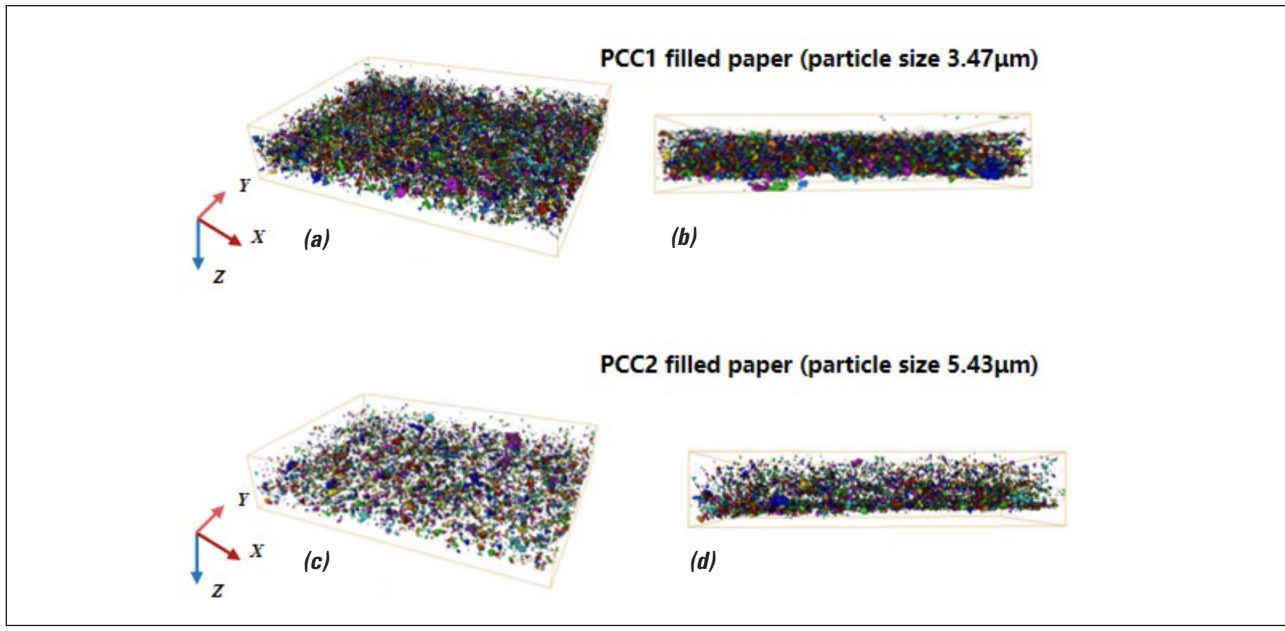

12. Three-dimensional (3D) distribution of filler particles in paper: (a) 3D view of PCC1 filled paper; (b) x–z view of PCC1 filled paper; (c) 3D view of PCC2 filled paper; and (d) x–z view of PCC2 filled paper.

majority of PCC1 and PCC2 filler particles possess a volume below 100 μm³. In addition, the comparison of specific surface areas (Fig. 11c) of fillers reveals that the smaller PCC1 filler particles exhibit a larger overall specific surface area. A large specific surface area is advantageous for enhancing the binding between filler and fiber, mitigating the negative impact of filling on strength properties [24]. However, the tight binding may consequently lead to a reduction of paper porosity.

To analyze the 3D distribution of filler particles within the paper, Avizo software was utilized to visualize their spatial distribution by the X-CT scanning images. As illustrated in **Fig. 12**, the PCC1 filled paper contains smaller and more numerous filler particles, whereas the PCC2 filler particles demonstrate larger ones. The PCC2 is predominantly concentrated near the bottom part of paper, while the PCC1 is relatively uniformly distributed.

To further quantify the filler distribution within the paper interior, the centroid positions of filler particles are estimated along the *x*, *y*, and *z* axes. The results presented in **Figs. 13a–13b** indicate that both the PCC1 and PCC2 fillers are relatively evenly distributed along the *x* and *y* axes. However, notably along the *z* axis, as shown in Fig. 13c, both filler distributions initially increase with the increasing *z*-depth, and then rapidly diminish near the middle bottom of paper with a turning point of approximate depth of 180 μm, signifying a lower filler concentration on the paper surfaces and a relatively higher concentration in the middle bottom of the paper. These observations in Fig. 13 can be interpretated such that compared with pulp fibers, the filler particles with higher density generally approach the forming wire earlier during the paper forming process. However, due to its small particle size, it is rather difficult for it to be retained alone on the forming wire. Once a fiber mat forms on the forming wire, the fillers start accumulating, and owing to its high specific gravity, the filler settles rapidly, resulting in a relatively high filler content at the bottom part of the paper. The aforementioned explanation can interpret the observation in Fig. 13c that compared with PCC1, the larger particle size of PCC2 facilitates its faster sedimentation, leading to a more pronounced accumulation near the bottom part of paper.

Permeation simulation

Using the method described in the Three-Dimensional Modeling and Numerical Simulation Methods section about the permeability simulation, simulations for the three prepared paper samples were conducted in the thickness and horizontal directions, respectively. The simulation results are discussed with regard to the aspects of permeation flow and pressure drops within the paper samples.

Case 1: Permeation simulation in the thickness direction

As depicted in **Figs. 14a–14b**, the streamline distributions in the unfilled paper and PCC2 filled paper (with large filler particles) are relatively straight, indicating their lower pore tortuosity. In contrast, the streamlines in the PCC1 filled paper (with small filler particles) are highly curved, suggesting that the addition of small PCC1 filler particles complicates the paper pores, elongates the fluid flow path, and impedes the fluid permeation. As depicted in Fig. 14b, the unfilled paper and PCC2 filled paper contain numerous high-velocity flow regions (indicated by red streamlines), which can be attributed to the larger pore (unfilled 7.12 μm;

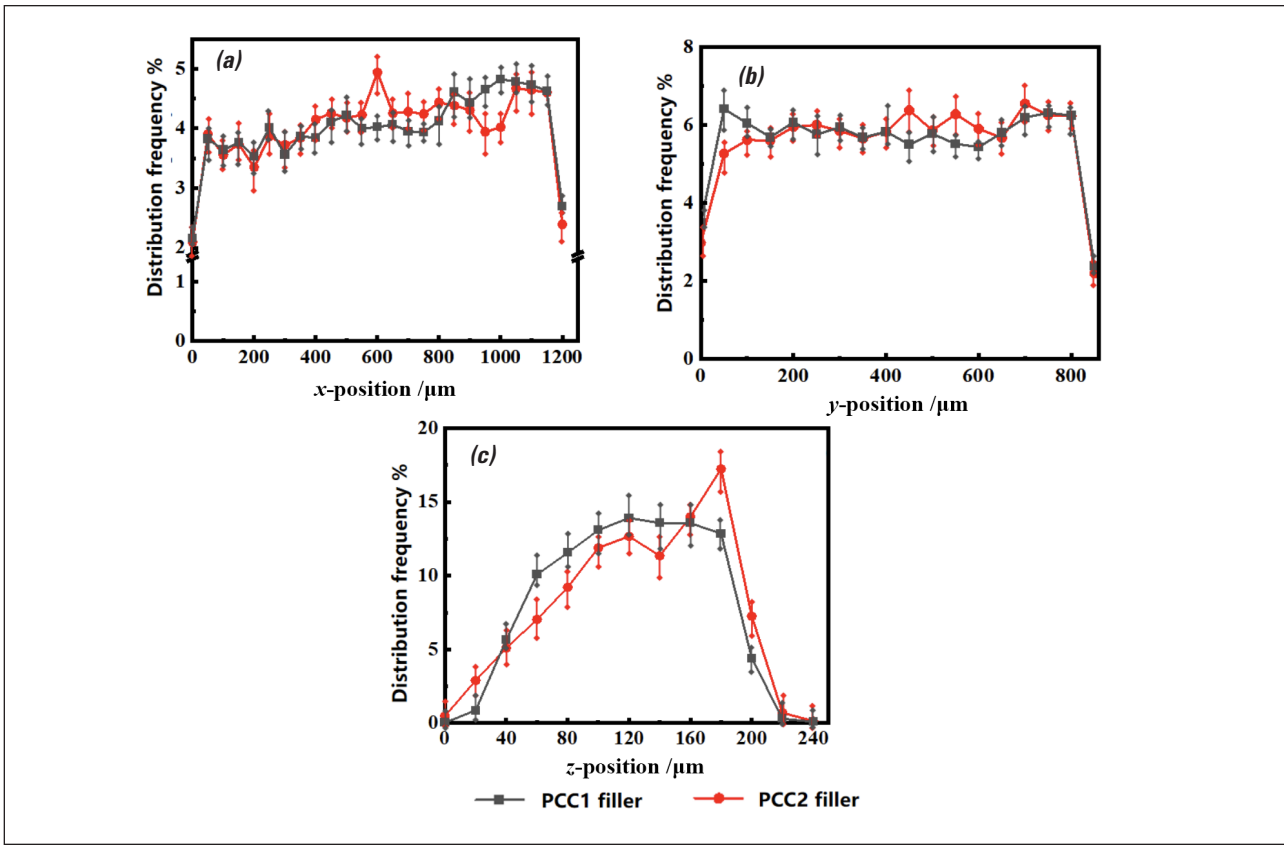

13. Distribution of the centroid positions of filler particles within the paper interior.

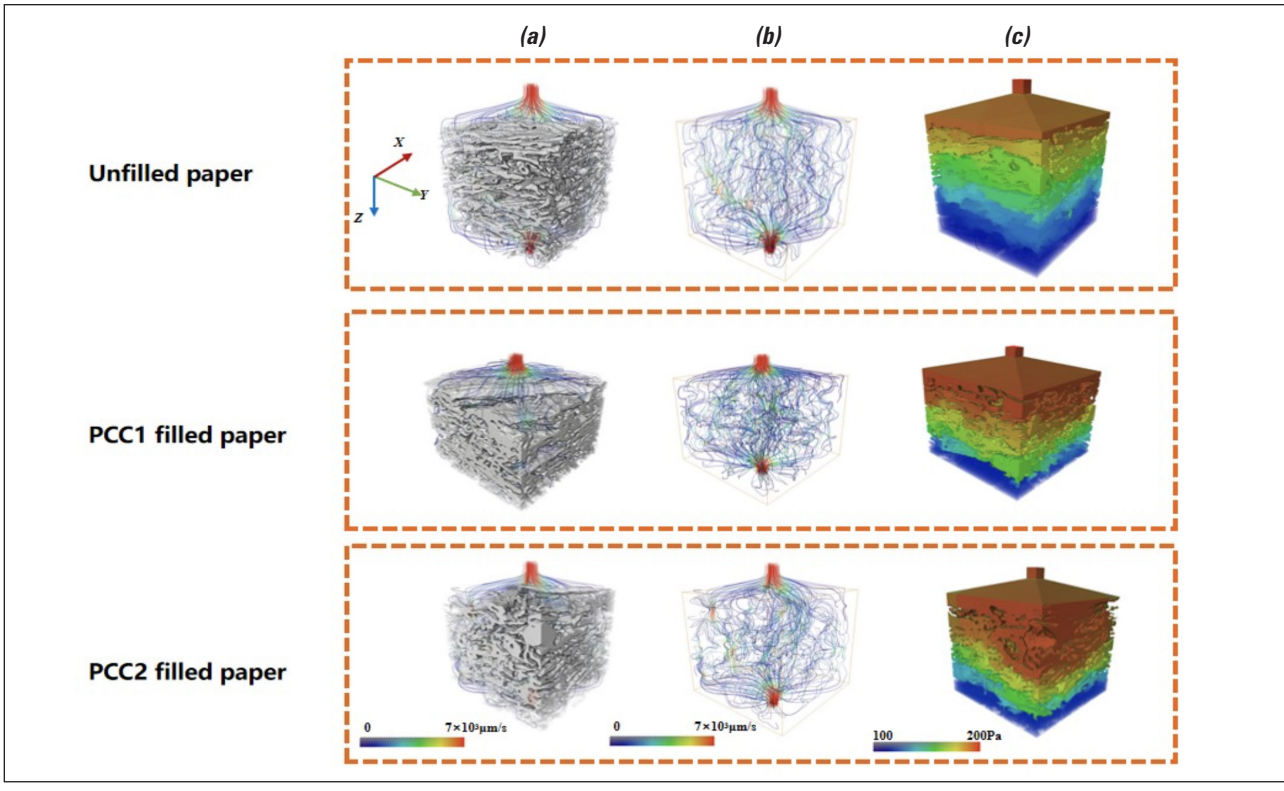

14. Simulated permeation flow lines and pressure drops in the thickness direction of paper samples: (a) permeation flow line in fiber phase; (b) permeation flow line in pore phase; and (c) pressure drop in fiber phase.

PCC2 7.50 μm) or pore throat sizes (unfilled 4.27 μm; PCC2 4.22 μm) in these paper samples.

As for the pressure drops within the paper samples in Fig. 14c, it can be seen that the pressure distribution of the unfilled paper is relatively uniform among the three samples, indicating that its pore structure is relatively uniform along the thickness direction. However, in the PCC2 filled paper, the pressure distribution undergoes significant variations near the paper bottom, which correlates with its filler distribution within the paper. As displayed in Fig. 12d, the filler in the PCC2 filled paper is more concentrated near the bottom, filling the pores and reducing the porosity and pore size, which in turn increases its fluid flow resistance and causes a rapid pressure drop. As for the PCC1 filled paper with small filler particles, the filler is more uniformly distributed along the thickness direction (Fig. 12b), resulting in a lower overall porosity (Table III). Consequently, the fluid encounters substantial resistance upon entering the paper interior, leading to an immediate pressure decline and a relatively uniform pressure distribution.

Based on the simulated permeation, the absolute permeability K of the determined RVE can be solved according to Darcy's Law, Eq. 3:

$$K = \frac{Q \cdot l}{A(P_{inlet} - P_{outlet})} \tag{3}$$

where Q represent the mass flow rate, l is the permeation path length, A is the cross-sectional area perpendicular to the fluid direction, and P_{inlet} and P_{outlet} are the pressures at the inlet and outlet, respectively.

The Kozeny-Carman (K-C) equation [25] is generally applicable to the calculation of creeping flow in porous media [26], which refers to the flow with a relatively low velocity and a Reynolds number less than 1. As shown in Eq. 4, the absolute permeability is described as a function of porosity and the specific surface area of the medium:

$$K = \frac{\phi^3}{c(1-\phi)^2 S^2} \tag{4}$$

where ϕ is the porosity of the porous medium, S is the specific surface area of the porous medium, and c is the coefficient related to the pore structure.

Referring to the reports of Fu [27] and others, the K-C equation for the randomly arranged fibrous porous media is:

$$K = \frac{{d_f}^2}{61.1(1-\phi)^{\frac{2}{3}}(1+347(1-\phi)^3)} \tag{5}$$

where ϕ is the porosity of the porous medium, and d_f is the experimental value of the cotton fiber diameter in the literature [28].

Using Eqs. 3-5, the absolute permeabilities K_1 of the unfilled paper, PCC1 filled paper, and PCC2 filled paper are calculated and compared with the experimental permeabilities K_2 and the theoretical permeabilities K_3 by the modified K-C equation. The comparison results are presented in **Table IV**. It shows that the simulated permeability values (K_1) are consistent with the experimental values (K_2), validating the simulation method. The addition of small-sized fillers (PCC1) significantly reduces paper permeability, while larger fillers (PCC2) have a lesser impact, highlighting the critical role of filler size in determining the fluid transport properties of paper. In our previous research, Xu reported that the absolute permeability of unfilled paper was 1.70 μm² in the thickness direction [29]. This indicates that the addition of fillers, especially small-sized fillers, significantly reduces the permeability in the thickness direction. These study results are also consistent with Singh's finding that the addition of PCC and kaolin particle fillers at certain concentrations leads to a decrease in permeability [14].

Case 2: Permeation simulation in the horizontal direction

To investigate the impact of filling on the horizontal permeation performance of paper, permeation simulations in the horizontal direction (x-direction) were further conducted for the unfilled paper, PCC2 filled paper, and PCC1 filled paper. **Figure 15** presents the x-direction simulation streamline and pressure diagrams for the three paper samples. As observed, the internal streamlines of all three pa-

Sample	Simulated Permeability K_1, μm²	Experimental Permeability K_2, μm²	Theoretical Permeability K_3, μm²
Unfilled paper	1.97	1.88	2.65
PCC1 filled paper	0.32	0.28	1.14
PCC2 filled paper	0.48	0.45	1.35

IV. Comparison of absolute permeability of paper samples in the thickness direction (PCC: precipitated calcium carbonate).

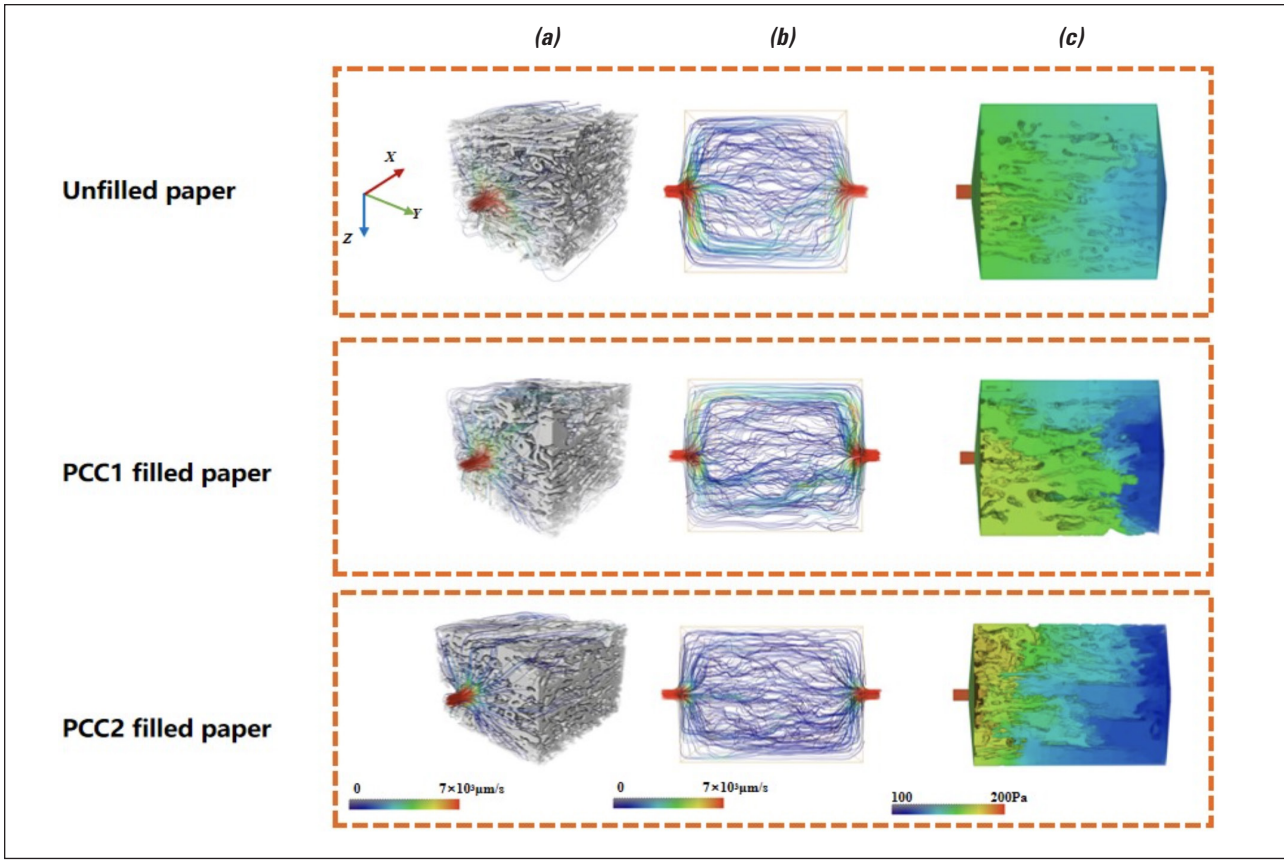

15. Simulated permeation flow lines and pressure drops in the horizontal direction of paper samples: (a) permeation flow line in fiber phase; (b) permeation flow line in pore phase; and (c) pressure drop in fiber phase.

pers are more uniformly distributed compared to those in the thickness direction, indicating a more homogeneous pore distribution in the *x*-direction.

It should be mentioned that, in contrast to the simulation results in the thickness direction, as shown in Fig. 15c, the pressure distributions in the horizontal direction are relatively uniform. However, the filling operation still causes a more pronounced pressure drop in the paper, and the filler distribution renders the internal pore structure less uniform, affecting the lateral fluid permeation. Comparing Fig. 14 and Fig. 15, it is obvious that the impact of filling on the permeation performance in the thickness direction is more substantial than that in the horizontal direction.

CONCLUSIONS

In this study using cotton linter pulp and precipitated calcium carbonate (PCC) filler as raw materials, the pure fiber paper and PCC1 and PCC2 filled papers (with different filler particle size) were prepared, followed by scanning with X-CT equipment. The experimental parameters (porosity, tortuosity, and fractal dimension) of the pore structure of paper samples were firstly characterized by MIP. Secondly, their 3D microstructures were constructed based on the X-CT slice images, the parameters of the constructed structures were estimated, and the filler characteristic parameters and 3D distribution were further characterized quantitatively. Eventually, the permeation simulations for three paper samples were conducted in the thickness and horizontal directions. The following remarks can be concluded:

1. The filling alters the paper porosity. Pore tortuosity differs by direction; the horizontal values are lower than those in thickness direction, showing filler distribution affects pore structure.
2. The estimated pore-throat radius distribution peaks for all paper samples are in the range of 3–5 μm, and that of the PCC1 filled paper with small filler particles increases to 1–5 μm, making it more uniform and tightening the paper structure.
3. The PCC1 filler with small particles is evenly distributed in paper samples, while PCC2 filler with big particles concentrates near the paper bottom. Both fillers distribute evenly along the horizonal direction. However, notably along the thickness direction, their distributions initially increase with the increasing *z*-depth, and then rapidly diminish near the middle bottom of paper.
4. Permeability of paper differs in directions. In the thickness direction, unfilled and PCC2 filled paper with big filler particles had relatively straighter stream-

lines and higher permeability than that of PCC1 filled paper, revealing that small-sized filler tends to hinder fluid penetration. Compared with the thickness direction, filling has a tiny impact on horizontal permeability, indicating the effect of directional differences in filler distribution on paper permeability.

This simulation-based approach provides a viable methodology for analyzing the effects of additives in materials, contributing to understanding the relationship between structure and performance of materials.

ACKNOWLEDGMENTS

The authors appreciate the support provided by State Key Laboratory of Advanced Papermaking & Paper-based Materials (2024ZD08), National Key Research and Development Program of China (2022YFF0607201), and Guangdong University Young Innovative Talents Program Project, China (2024KQNCX086).

LITERATURE CITED

1. Ling, H., Wang, L., et al., *Carbohydr. Polym.* 312: 120794(2023). https://doi.org/10.1016/j.carbpol.2023.120794.
2. Qi, X., *Printing Materials and Their Properties*, 2nd edn., China Print & Publishing House, Beijing, 2008.
3. Qian, X., *Modification Technology of Papermaking Fibers and Fillers*, Chemical Industry Press, Beijing, 2011.
4. Puurtinen, A., *Appita J.* 57(3): 204(2004).
5. Roux, S., Feugeas, F., Bach, M. et al., *J. Microsc.* 229(1): 44(2008). https://doi.org/10.1111/j.1365-2818.2007.01864.x.
6. Li, J., Shen, W., Guo, Q., et al., *Chin. J. Pulp Pap.* 39(6): 29(2020).
7. Villarraga-Gomez, H., Herazo, E.L., and Smith, S.T., *Precis. Eng.* 60: 544(2019). https://doi.org/10.1016/j.precisioneng.2019.06.007.

ABOUT THE AUTHORS

The elements of fillers play an important role in paper's 3D structure and performance. Investigating the 3D structure of filled paper lays a foundation for understanding its structure-performance relationship. Previous studies focused more on wet paper webs rather than investigating the relationship between fillers in dried paper and their permeability performance as we have done here.

The most difficult aspect of this study was in 3D model parameter extraction and permeability simulation. The work was successfully accomplished through the precise separation of the three components (filler, fiber, and pore) and the scientific setting of the conditions for permeability simulation.

It was surprising to find that fillers have different distribution characteristics in the paper samples. Moreover, the paper permeability varies in different directions, with small-sized filler having a significant impact on fluid penetration in the thickness direction. Compared with in the thickness direction, filling has a tiny impact on the horizontal permeability, indicating the effect of directional differences in filler distribution on paper permeability.

This research offers an effective exploratory approach for investigating paper fillers from the perspective of computer simulation, facilitating the structural design and performance optimization of paper-based functional materials. Our next step is to add force fields in simulation, improving the application scope of this research.

J. Chen

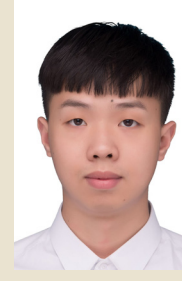

Wang

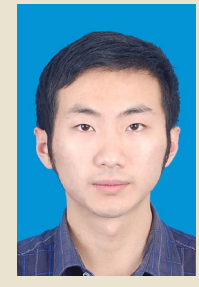

Liu

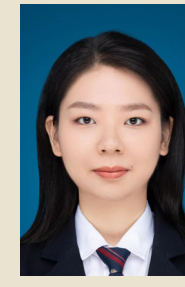

L. Chen

Shen

Simon

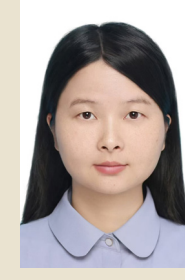

Huang

J. Chen is a graduate student, Wang is a graduate, L. Chen is a master's student, and Shen is a professor at the State Key Laboratory of Advanced Papermaking & Paper-based Materials, South China University of Technology, in Guangzhou, Guangdong, P.R. China. Liu is associate professor with the School of Art and Media, Guangzhou Vocational and Technical University of Science and Technology, in Guangzhou, Guangdong, P.R. China. Simon is professor of Computational Applied Mechanics at the University of Wuppertal in Wuppertal, Germany. Huang is professor in the School of Computer Science and Engineering, South China University of Technology, in Guangzhou, Guangdong, P.R. China. Email Shen at ppwhshen@scut.edu.cn.

8. Axelsson, M. and Svensson, S., *Pattern Anal. Appl.* 13(2): 159(2010). https://doi.org/10.1007/s10044-009-0146-1.
9. Preston, J., Toivakka, M., Heard, P., et al., "Visualisation, modeling and image analysis of coated paper microstructure: Particle shape microstructure interrelations," *Int. Papermaking Environ Conf., Proc., Books A and B*, Åbo Akademi University, Turku, Finland, 2008, pp. 19-832.
10. Samuelsen, E.J., Gregersen, Ø.W., Houen, P.J., et al., *J. Pulp Pap. Sci.* 27(2): 50(2001).
11. Al-Qararah A.M., Ekman, A., Hjelt, T., et al., *Colloids Surf., A* 482: 544(2015). https://doi.org/10.1016/j.colsurfa.2015.07.010.
12. Ramaswamy, S., Huang, S., Goel, A., et al., "The 3D structure of paper and its relationship to moisture transport in liquid and vapor forms," in *The Science of Papermaking, Trans. of the XIIth Fund. Res. Symp. Oxford, 2001*, (C.F. Baker, Ed.), FRC, Manchester, 2018, pp. 1289-1311. https://doi.org/10.15376/frc.2001.2.1289.
13. Lavrykov, S., Ramarao, B.V., and Evans, D.B., "Permeability of pulps and fillers and their relationship to wet pressing," *6th PIRA Int. Conf. Wet End Chem., Proc.,* PIRA International, Leatherhead, UK, 2005.
14. Singh, R., Lavrykov, S., and Ramaro, et al., *Colloids Surf., A* 333(1-3): 96(2009). https://doi.org/10.1016/j.colsurfa.2008.09.035.
15. Huang, X., Wang, Q., Zhou, W., et al., *Powder Technol.* 283: 618(2015). https://doi.org/10.1016/j.powtec.2015.06.015.
16. Brun, E., Vicente, J., Topin, F., et al. *Adv. Eng. Mater.* 11(10): 805(2009). https://doi.org/10.1002/adem.200900131.
17. Wang, Y., Liu, Y., Xu, J., et al., *Cellulose* 31(1): 187(2021). https://doi.org/10.1007/s10570-023-05645-3.
18. Liu, Y., Zhang, W., Liang, X., et al., *Rock and Soil Mechanics* 40(7): 2723(2019).
19. Chwang, A.T. and Chan, A.T., *Annu. Rev. Fluid Mech.* 30(1): 53(1998). https://doi.org/10.1146/annurev.fluid.30.1.53.
20. Sander, R., Pan, Z., Connell, L.D., et al., *J. Nat. Gas Sci. Eng.* 37: 248(2017). https://doi.org/10.1016/j.jngse.2016.11.041.
21. Discacciati, M. and Quarteroni, A., *Rev. Mat. Complut.* 22(2): 315(2009). https://doi.org/10.5209/rev_REMA.2009.v22.n2.16263.
22. Monteleone, A., Monteforte, M., and Napoli, E., *Comput. Fluids* 159: 9(2017). https://doi.org/10.1016/j.compfluid.2017.09.011.
23. Fan, N., Wang, J., Deng, C., et al., *J. Nat. Gas Sci. Eng.* 81: 103384(2020). https://doi.org/10.1016/j.jngse.2020.103384.
24. Lourenço, A.F., Godinho, D., Gamelas, J.A.F., et al., *Cellulose* 26(5): 3489(2019). https://doi.org/10.1007/s10570-019-02303-5.
25. Carman P.C., *Trans. Inst. Chem. Eng.* 15: 150(1937).
26. Kozeny, J., *Sitzungsber. Akad. Wiss. Wien, Math.-Naturwiss. Kl.* 136: 271(1927).
27. Fu, H.M., Xu, F.F., abd Li, Y., *J. Huaqiao Univ., Nat. Sci.* 33(5): 535(2012).
28. Wu, Y.Q., Zhao, X.X., Liu, G., et al. *Quality and Technical Supervision Research* (6): 27(2011).
29. Xu, J., "Three-dimensional characterization of paper pore structure and permeability simulation based on X-ray computed tomography," Master's thesis, South China University of Technology, Guangzhou, Guangdong, China, 2022.

ABOUT THIS PAPER

Cite this article as:
Chen, J., Wang, Y., Liu, Y., et al., *TAPPI J.* 25(3): 153(2026). https://doi.org/10.32964/TJ25.3.153

DOI: https://doi.org/10.32964/TJ25.3.153

ISSN: 0734-1415

Publisher: TAPPI Press

About this journal